Intermetallics 142 (2022) 107443

Contents lists available at ScienceDirect

Intermetallics

journal homepage: www.elsevier.com/locate/intermet

On intermetallic phases formed during interdiffusion between aluminium alloys and stainless steel

Tina Bergh [a,*], Siri Marthe Arbo [b,c], Anette Brocks Hagen [d], Jørgen Blindheim [e], Jesper Friis [a,d], Muhammad Zeeshan Khalid [f], Inga Gudem Ringdalen [d], Randi Holmestad [a], Ida Westermann [b], Per Erik Vullum [a,d]

[a] Department of Physics, Norwegian University of Science and Technology (NTNU), Høgskoleringen 5, 7491, Trondheim, Norway
[b] Department of Materials Science and Engineering, NTNU, Alfred Getz vei 2, 7491, Trondheim, Norway
[c] SINTEF Manufacturing AS, 2831, Raufoss, Norway
[d] SINTEF Industry, 7034, Trondheim, Norway
[e] Department of Mechanical and Industrial Engineering, NTNU, Richard Birkelands vei 2b, 7491, Trondheim, Norway
[f] Department of Manufacturing and Civil Engineering, NTNU, Teknologiveien 22, 2815, Gjøvik, Norway

ARTICLE INFO

Keywords:
Stainless steel
Aluminium-steel joining
Intermetallic phases
Transmission electron microscopy
Density functional theory
Nanoindentation

ABSTRACT

One of the major challenges in welding of aluminium (Al) alloys and steels is the growth of brittle intermetallic phases, which depends on the thermomechanical processing history and the alloying elements. This work focuses on the intermetallic phase layers formed in roll bonded composites of Al alloy 6082 and stainless steel 316L after interdiffusion at temperatures in the range of 400 – 550 °C. Scanning and transmission electron microscopy characterisation showed that during interdiffusion, an α_c-$Al_{15}(Fe,Cr,Mn)_3Si_2$ phase layer formed first, before a discontinuous layer of τ_1-$FeNiAl_9$ formed at the Al-α_c interface. Subsequently, a layer of θ-Fe_4Al_{13} and τ_{11}-Al_5Fe_2Si formed at the α_c-steel interface, followed by a layer of η-Fe_2Al_5 with precipitates rich in Cr and Si or Ni. Nanoindentation and density functional theory calculations were performed to assess the mechanical properties of the formed phases. Miniature tensile testing confirmed that the bond strength decreased as the thicknesses of brittle phase layers increased. Further, it was found that the growth rate of the total intermetallic phase layer was significantly reduced for the high alloyed 6082-316L composites compared to unalloyed reference composites of 1080-S355. Altogether, this work provides insight into the combined effects of the alloying elements Si, Mn, Cr and Ni on the formation, growth and mechanical properties of the interfacial intermetallic phases in Al-steel joints.

1. Introduction

The use of joints between aluminium (Al) alloys and steels in structural components enables improved strength to weight distribution. Al-steel joints can be beneficial, for instance in automobiles, since they may facilitate improvements of the energy efficiency. However, there are several challenges with welding of dissimilar metals, and growth of intermetallic phases (IMPs) is a major one. During Al-steel welding, elevated temperatures are typically reached, which promote interdiffusion. Subsequently, formation and growth of IMPs occur, due to the low solid solubility of iron (Fe) in Al [1]. The IMPs are inherently brittle, and porosity may form as they grow [2]. Consequently, excessive growth of IMPs typically leads to strength reduction and interfacial fracture during loading [2–6]. Therefore, it is important in Al-steel joining to understand both the mechanisms that govern IMP growth, and how the formed IMPs impact the joint properties.

The formation and growth of IMPs are governed both by the thermomechanical processing history and the chemical compositions of the used alloys. In general, increasing heat input leads to thicker interfacial IMP layers, since the growth is predominantly diffusion controlled [7,8]. In joints of low-alloyed Al and steel, θ-Fe_4Al_{13} ($FeAl_3$) and subsequently η-Fe_2Al_5 form at the bonded interfaces [7,9]. With time at elevated temperatures, η dominates the IMP layer growth and typically develops an irregular saw-tooth morphology with columnar grains [6,10]. Al-Fe phases richer in Fe may also form with prolonged heat treatments or at higher temperatures [8], while metastable phases have been reported

* Corresponding author.
E-mail address: tina.bergh@ntnu.no (T. Bergh).

https://doi.org/10.1016/j.intermet.2021.107443
Received 23 July 2021; Received in revised form 14 December 2021; Accepted 14 December 2021
Available online 27 December 2021

for high cooling rates [11]. However, the presence of alloying elements in the steel and/or the Al alloy can markedly alter the IMP phase formation sequence and growth rate.

When it comes to alloying elements, Al alloys with silicon (Si) have been studied extensively since Si has been found to notably reduce the IMP growth rate [12–19]. Presence of Si may result in formation of an Al-Fe-Si IMP layer that acts as a diffusion barrier to Fe and thereby reduces the IMP growth rate [14]. Several Al-Fe-Si phases have been described [20–22], and various of these have been identified in joints. Most often, the α_h-$Al_{7.1}Fe_2Si$ (τ_5) phase [18,19,23] or the β-$Al_{4.5}FeSi$ (τ_6) phase [2,19,23] has been reported to form first at Al-Fe interfaces. For prolonged IMP layer growth, growth of the Al-Fe-Si phase(s) is typically followed by growth of the θ and η phases [14,17], which then contain minor amounts of Si [24]. Other Al-Fe-Si phases have also been identified [19,23,25,26]. The formation of IMPs may however, be influenced by alloying elements that are only present in minor amounts. One example is that the presence of certain transition elements *M*, e.g. Mn and Cr, lead to formation of the α_c-$Al_{15}(Fe, M)_3Si_2$ phase instead of the otherwise expected α_h phase [27–29]. The α_c phase has been observed in Al-steel joints both where the Al alloy contained Mn and/or Cr [17,30,31] and where the steel contained Cr [25]. This advocates the importance of studying the combined effects of alloying elements contained within both the Al alloy and the steel, to gain further insight into IMP formation and growth.

When it comes to steels, stainless steels are widely used due to their high strengths and superior corrosion resistances. These contain considerable amounts of Cr and often Ni, which reduce the IMP growth rates [25,32,33]. Previous studies have reported that the θ and η phase layers can incorporate both Cr and Ni [33–36], and various Al-Ni(-Fe) [11,33,37]or Al-Cr phases [38,39] have been identified at Al-steel interfaces. More research is needed to fully understand the effect of Ni and Cr additions and their interplay with other alloying elements.

This study concerns the combined effects of the alloying elements Cr, Ni, Si and Mn contained within a commonly used stainless steel and a widely used Al alloy, on the IMP formation and layer growth. The formed interfacial IMPs are assessed in terms of morphology, chemical composition and crystal structure, using electron microscopy techniques. Their mechanical properties are evaluated by first principles calculations, nanoindentation and miniature tensile testing. Together the findings give insights into how heat treatments and alloying elements affect welds of Al alloys and stainless steels, which may be valuable for fabrication of improved Al-steel joints using a wide range of welding methods.

2. Materials and methods

2.1. Materials, roll bonding procedure and heat treatments

The starting materials were 1 mm thick sheets of Al alloy 6082-T4 and stainless steel 316L. For reference, sheets of industrially pure Al 1080 and low-alloyed and low-carbon structural steel S355 were used. The nominal compositions are given in Table 1.

The sheets were cut into specimens for rolling, measuring 15 × 120 × 1 mm. The specimens were degreased with acetone and brushed in the direction transverse to the rolling direction, using a rotating steel wire brush with a wire diameter of 0.3 mm. Subsequently, the surfaces were cleaned with compressed air to remove loose particles resulting from brushing. The specimens were then stacked to create three-layered composites with the stacking sequence steel-Al-steel, and fastened with Al rivets in the front and rear end to prevent lateral movement during rolling. Each composite was heat treated for 10 min in an air furnace to reach the desired rolling temperature of 150 °C. Immediately after heat treatment, each composite was rolled in a single pass. The thickness reductions were measured to be in the range of 50 – 55%.

To study the formation and growth of IMPs, the rolled composites were cut into ~10 mm long pieces, before they were subjected to various heat treatments. The heat treatments were conducted in salt baths for temperatures in the range of 400 – 550 °C and for times in the range of 2 – 240 min, followed by water quenching.

2.2. Scanning electron microscopy

SEM was performed on ground and polished metallographic cross-sections of the heat treated composite pieces. A field emission gun (FEG) Zeiss Gemini Ultra 55 microscope was used to capture SEM images using a secondary electron (SE) and a backscatter electron (BSE) detector, and the microscope was operated at 10 kV. The interfacial IMP layers that had formed were identified and their respective thicknesses measured.

2.3. Transmission electron microscopy

TEM lamellae were fabricated by focused ion beam (FIB) lift-out using a FEI Helios G4 FIB-SEM. Lamellae were prepared from 6082-316L composites heat treated at 500 − 550 °C for various times. To assess the crystal structures of the formed phases, selected area electron diffraction (SAED) and precession electron diffraction (PED) were performed using a JEOL JEM-2100F equipped with a Nanomegas ASTAR system. For PED, the microscope was operated at 200 kV in nano-beam diffraction mode with a convergence angle of 1.0 mrad and a precession angle of 21 mrad. Zone-axis SAED and PED patterns were acquired on an Ultrascan camera fitted to the microscope. Scanning TEM (STEM) and X-ray energy dispersive spectroscopy (EDS) were performed using a cold FEG JEOL ARM 200CF microscope, operated at 200 kV. The EDS maps were analysed using the python library hyperspy [40]. For each map, the spectra were first binned in the spatial axes, before model fitting was performed spectrum by spectrum, with a model comprising one Gaussian per X-ray line and a sixth order polynomial to model the background. Quantification was performed by the Cliff-Lorimer method using calculated *k*-factors. The compositions of individual IMP layers were estimated by summing the spectra within single phase regions and performing model fitting and quantification of the summed spectra.

2.4. Density functional theory calculations

To assess the mechanical properties of the individual IMPs identified by TEM in their pure bulk form, density functional theory (DFT) simulations were performed using the Vienna ab-initio Simulation Package (VASP) [41]. The atomic structures that were used in the DFT calculations are given in the supplementary information (SI) Section S1. The Perdew-Burke-Ernzerhof generalised gradient approximation exchange correlation functional and the projector augmented-wave method were used [42,43], and the calculations were performed spin-polarized. The plane-wave energy cutoff was set to 500 eV, and a gamma sampling of

Table 1
Nominal compositions of the used 1080 and 6082 Al alloys, stainless steel 316L and structural steel S355 in wt.%.

Alloy	Al	Fe	Cr	Ni	Mo	Mn	Mg	Si	Ti	C	Cu
1080	99.8	–	–	–	–	–	–	–	–	–	
6082	Bal.	0.29	–	–	–	0.58	1.00	0.90	0.04	–	0.01
316L	–	Bal.	16.65	10.06	2.025	1.30	–	0.34	–	0.022	–
S355	0.05	Bal.	0.03	0.03	–	0.62	–	0.01	–	0.07	–

k-points was used with a maximum distance in the range of 0.18 – 0.70 $Å^{-1}$. Formation enthalpies of selected phases were calculated with solid solution in Al as the reference. The elastic stiffness tensors for each phase were calculated within VASP by performing finite distortions of the lattice and deriving the elastic constants from the stress-strain relationship. Independent elastic constants were calculated based on the crystal symmetries and by following the elastic stability criteria for the relevant crystal systems [44]. Subsequently, elastic properties were calculated based on the Voigt-Reuss-Hill averaging method [45].

2.5. Nanoindentation

Nanoindentation was performed on a specimen heat treated at 550 °C for 180 min, to assess the mechanical properties of the individual IMP layers. A Hysitron Tribo-Indenter TI 950 with a maximum load force of 3 mN and a Berkovich indenter tip with a semi-angle of 65.3°, were used for indentation. The hardnesses and moduli were calculated from the indentation curves following the Oliver-Pharr method [46]. The indents were post-inspected by SEM, for which a dual-beam FEI Helios G4 FIB-SEM was used and operated at 10 kV.

2.6. Tensile testing

To assess the bond strengths of the heat treated Al-steel interface regions, miniature tensile testing was performed using the setup developed by Blindheim et al. [47]. Three samples were selected for tensile testing, and these were composites heat treated at 500 °C for 180 min, 550 °C for 10 min and 550 °C for 60 min. Miniature cylindrical specimens consisting of a reduced section (⌀ 1.0 mm) and shoulder sections (⌀ 1.9 mm), were produced by milling using a Mazak 3-axis vertical machining centre. Fig. 1(a) and (b) show schematic illustrations of the specimens. To enable testing of only one of the two Al-steel interfaces in one composite at a time, the specimens were fabricated so that one Al-steel interface was located in the reduced section of the specimen, while the other was located in the upper shoulder region. Each composite sheet was bonded to a larger steel piece for fixture during milling, with Master Bond EP15ND-2 one-component epoxy cured at 155 °C for 1.5 h. For tensile testing, a specially designed split collar was used to grip the upper shoulder of the specimens, whereas the other end of the specimen remained fixed to the steel piece, as depicted in Fig. 1(b). The applied load and total displacement were recorded at a sampling frequency of 10 Hz, using a MTS Criterion Model 42 ball screw universal testing machine, with the cross-head speed set to 1 mm/min. The resulting fracture surfaces were imaged by SEM using a Zeiss Supra 55 VP operated at 10 kV.

3. Results

3.1. Scanning electron microscopy

The total interfacial IMP layer thickness was measured by SEM for the 1080-S355 and 6082-316L composites subjected to various heat treatments. The total thickness is plotted versus the square root of the heat treatment time in Fig. 2. Fig. 2(a) presents the results from the composites of the reference combination 1080-S355, while (b) shows the values measured for the 6082-316L composites. Directly after rolling, no IMP layer could be discerned by SEM in neither the 1080-S355 nor the 6082-316L composites. Previous studies have shown that interfacial Al-Fe IMPs mainly follow diffusion limited growth characteristics [2,7,8]. In that case, a parabolic relationship between layer thickening, Δx, and heat treatment time, t, is expected, which is given by: $\Delta x = \sqrt{kt}$, where k is a temperature dependent rate constant [48]. Therefore, linear regression was performed on the measured values, and the resulting fit lines are shown in Fig. 2. The rate constants obtained for the 1080-S355 composites were respectively 0.43, 0.26, 1.17 and 2.59 $\mu m^2 s^{-1}$ at 400, 450, 500 and 550 °C. For the 6082-316L composites they were 0.003 and 0.439 $\mu m^2 s^{-1}$ at 500 and 550 °C, respectively. Evidently, the 6082-316L composites showed a prominent decrease in IMP growth rate compared to the 1080-S355 composites.

The 1080-S355 composites showed large local variations in IMP layer thickness that resulted in large standard deviation, as can be seen from the error bars in Fig. 2(a). Fig. 3(a) shows a SEM image of a 1080-S355 composite heat treated at 500 °C for 60 min, where a discontinuous IMP layer consisting of two individual layers, Layers i and ii, can be seen. SEM EDS spectra were acquired from points centred in each of the two layers, and quantification resulted in Al/Fe-ratios of 2.79 and 2.26, corresponding to the phases Fe_4Al_{13} and Fe_2Al_5 [1], respectively. The layer showed large thickness variations and an irregular interface towards the steel. The 6082-316L composites had continuous IMP layers showing less thickness variations, which gave smaller standard deviations. Fig. 3(b) displays a 6082-316L composite heat treated at 550 °C for 180 min. A continuous IMP layer can be seen, together with pores that formed along one part of the Al-IMP interface.

Further studies of the interfacial IMP layers focused on the 6082-316L composites heat treated at 550 °C, since heat treatments at this temperature resulted in substantial IMP growth. Fig. 3(c)–(g) present SEM images showing the individual interfacial IMP layers formed after increasing heat treatment times. A thin single IMP layer (Layer 1) formed after 2 min, as shown in (c). Two layers could be observed after 10 min, and the second layer (Layer 2) formed at the interface towards Al, as shown in (d). With increasing heat treatment time, a third and a fourth layer (Layer 3 and Layer 4) formed and the layers grew, as shown in (e)-(g).

3.2. Transmission electron microscopy

More detailed studies of the interfacial IMPs formed in the heat treated 6082-316L composites were conducted by TEM. Fig. 4(a) shows a bright field-(BF-)TEM image of the specimen heat treated for 2 min at 550 °C. A continuous IMP layer had formed that was in average 0.13 ± 0.05 μm thick and mainly consisted of a single phase layer (Layer 1). The individual grains in Layer 1 formed an irregular wavy interface to Al, while the interface to steel was flatter. Fig. 4(b) presents element maps based on STEM EDS. It can be seen that Layer 1 mainly consisted of Al, Fe and Si with smaller amounts of Cr and Mn. In addition, there was a Si-rich layer adjacent to steel that was ~10 nm thick. Numerous oxide

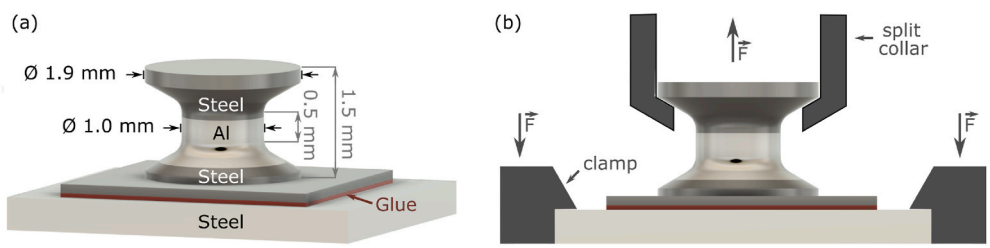

Fig. 1. Illustration of the miniature tensile testing. **(a)** A tensile testing specimen, where one of the Al-steel interface regions is located within the reduced section of the specimen. The dimensions are given. **(b)** Tensile testing using a split collar of one specimen that is fastened with clamps.

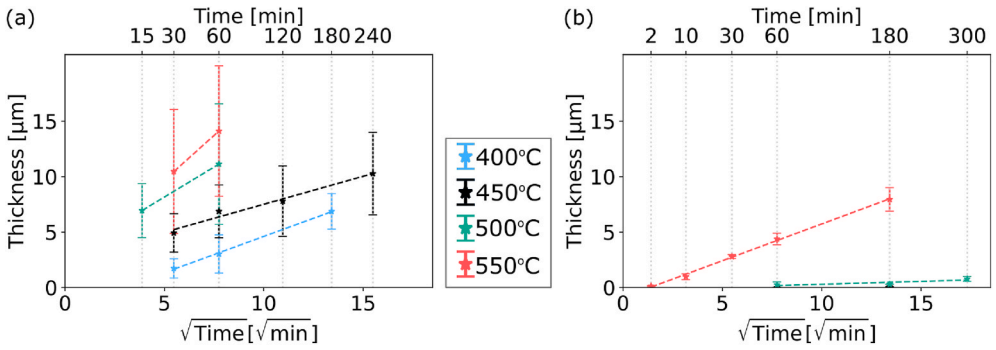

Fig. 2. The average thickness of the total IMP layer as a function of the square root of the heat treatment time, for alloy combinations **(a)** 1080-S355 and **(b)** 6082-316L, heat treated at 400, 450, 500 and 550 °C. The error bars show plus and minus one standard deviation based on ca. 20 individual measurements, and the dashed lines show fit lines obtained by linear regression.

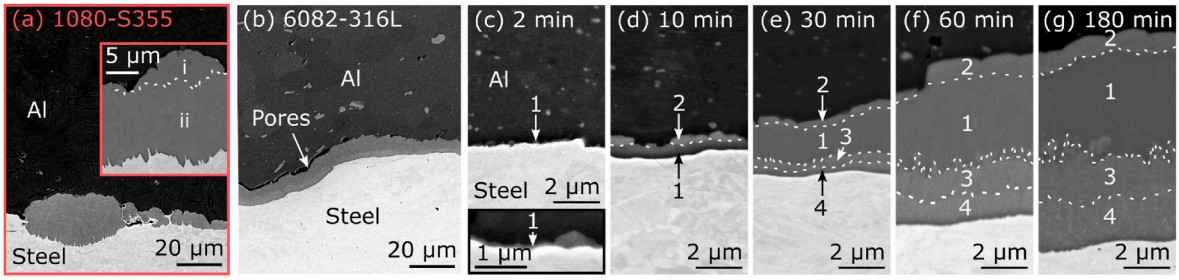

Fig. 3. Growth of interfacial IMP layers. SEM images showing a **(a)** 1080-S355 composite after 60 min at 550 °C and **(b)** 6082-316L composite after 180 min at 550 °C. SEM images showing 6082-316L composites after heat treatments at 550 °C for **(c)** 2 min, **(d)** 10 min, **(e)** 30 min, **(f)** 60 min and **(g)** 180 min. BSE SEM images are shown, with the exception of (a) (main image, not inset), (c) and (d), which show SE SEM images. Note that the insets in (a) and (c) show higher magnification SEM images of other areas than the main images. The dashed white lines indicate borders between distinct IMP layers denoted i – ii for 1080-S355 and 1 – 4 for 6082-316L.

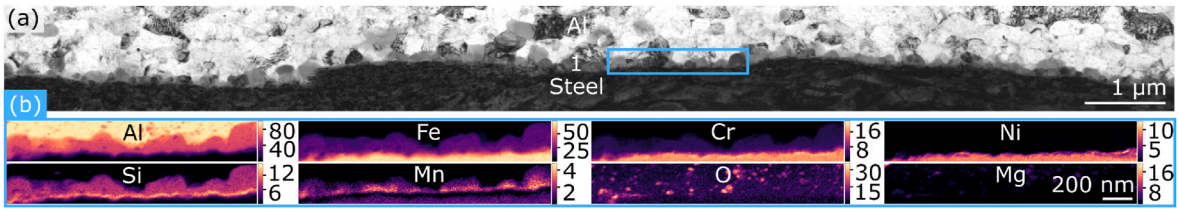

Fig. 4. The interfacial IMP layer after 2 min at 550 °C. **(a)** Overview BF-TEM image showing the first formed IMP layer (Layer 1). **(b)** Element maps (showing at.%) based on STEM EDS from the region outlined in blue in (a).

particles, composed of Al-O(-Mg) were located close to the Al-steel interface. The composition of Layer 1 was estimated based on STEM EDS data from several mapped regions, and the average composition is listed in Table 2. TEM characterisation was also done for a specimen heat treated for 180 min at 500 °C, as showed in SI S2. Here, Layer 1 was 0.25 ± 0.07 µm thick and showed close resemblance to that in the 550 °C 2 min specimen.

Table 2
Estimated compositions of the interfacial IMP layers, based on STEM EDS of lamellae from 6082-316L composites heat treated at 550 °C for 2 min, 10 min and 60 min. The relative compositions of the major constituting elements, Al, Fe, Cr, Ni, Si and Mn, are given in at.%. These compositions were subject to systematic errors emanating from the use of calculated *k*-factors and from absorption of low energy X-rays, and should be regarded as semi-quantitative values. The measured thicknesses are also listed.

Layer	Time [min]	Thickness [µm]	Al	Fe	Cr	Ni	Si	Mn
1	2	0.13	63	21	4	0.9	9	2
1	10	0.8	70	16	4	0.5	9	0.3
1	60	1.7	74	14	4	0.4	8	0.5
2	10	≲0.5	77	11	<0.1	10	2	<0.1
2	60	≲0.7	80	8	<0.1	11	1	<0.1
3	60	0.8	69	18	5	2	6	0.3
4	60	0.3–1.5	69	21	5	3	2	0.3

After 10 min at 550 °C, a second layer (Layer 2) had formed that can be seen in Fig. 5, where (a) shows a BF-TEM image. Layer 2 was discontinuous and included relatively large frequently faceted grains, typically up to ~0.5 µm thick. Element maps based on STEM EDS are shown in Fig. 5(b), and it can be seen that this layer consisted of Al, Fe and Ni with minor amounts of Si. Layer 1 had grown notably compared to after 2 min and had an average thickness of 0.8 µm. Also, the morphologies of Layer 1 grains had changed to elongated grains oriented normal to the Al-steel interface. The estimated average compositions of both layers are given in Table 2. For Layer 1, the composition was comparable to that after 2 min, except that the Mn content had decreased notably from ~2 at.% to <1 at.%.

The interfacial IMP layer in a composite heat treated at 550 °C for 60 min is shown in Fig. 6. Fig. 6(a) presents a BF-TEM image, (b) presents a HAADF-STEM image, and element maps based on STEM EDS are shown in (c). At this stage, four distinct IMP layers (Layers 1 – 4) could be seen.

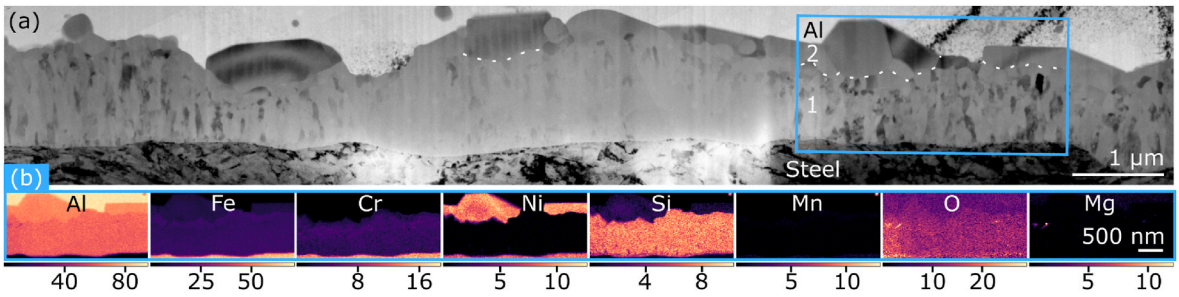

Fig. 5. The interfacial IMP layers after 10 min at 550 °C. **(a)** Overview BF-TEM image showing the interface region where two IMP layers (Layers 1 and 2) had formed. The dashed white lines mark some of the borders between the two. **(b)** Element maps (showing at.%) based on STEM EDS of the region outlined in blue in (a).

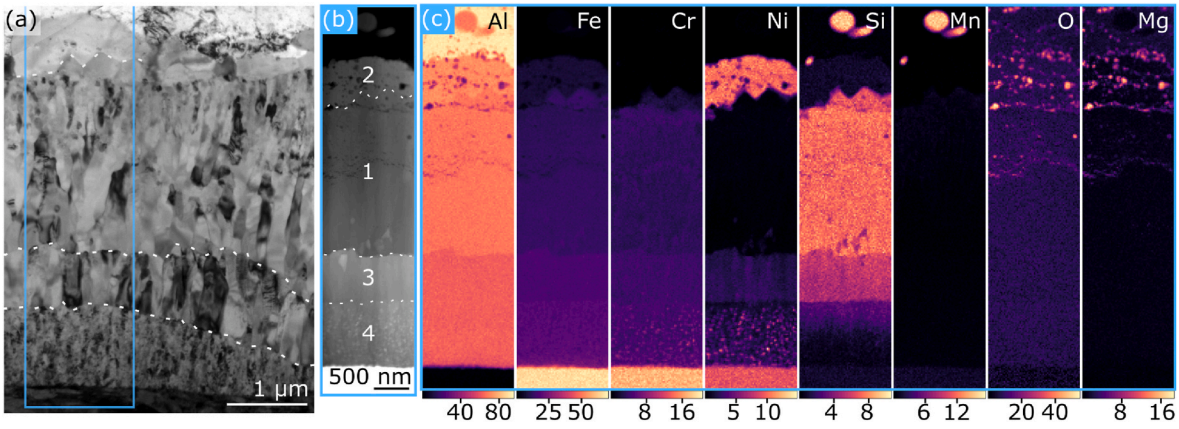

Fig. 6. The interfacial IMP layers after 60 min at 550 °C. **(a)** Overview BF-TEM image and **(b)** HAADF-STEM image of the region outlined in blue in (a), where the dashed white lines mark borders between each IMP layer (Layers 1 – 4). **(c)** Element maps (showing at.%) based on STEM EDS of the region shown in (b).

Layer 2, closest to Al, had grown slightly and consisted of Al-Fe-Ni grains typically up to ~0.7 µm thick. Layer 1 had grown notably and was in average 1.7 µm thick. Further, a third layer, (Layer 3) had formed that was in average 0.8 µm thick. Both Layers 1 and 3 consisted of elongated grains and were mainly composed of Al, Fe, Si and Cr. Layer 3 also contained a notable amount of Ni. A fourth layer had also formed (Layer 4) that showed a much more refined microstructure with thin elongated grains containing numerous small precipitates. Closer inspection by STEM EDS revealed that individual precipitates were either mainly composed of Ni or Cr with minor amounts of Si, both possibly also containing considerable amounts of Al and/or Fe. The thickness of Layer 4 showed large local variations and was measured to be in the range of 0.3 – 1.5 µm. The estimated compositions of the four layers are given in Table 2.

To assess the crystal structures of the IMPs, zone axis SAED and PED patterns were acquired from several IMP crystals in specimens that had undergone various heat treatments. Consistent results were obtained for Layers 1, 2 and 4, while Layer 3 showed local discrepancies for different lamellae. Patterns from Layer 1 could be indexed with respect to the cubic α_c phase ($Al_{15}(Fe,M)_3Si_2$, α-AlFeSi, $a = 12.56$ Å; $Im\bar{3}$ (204) [49]). Fig. 7(a) shows a PED pattern from an α_c crystal. The patterns from Layer 2 were consistent with the τ_1-Al_9FeNi phase ($a = 6.24$, $b = 6.30$, $c = 8.60$ [Å], $\beta = 95.1°$; $P2_1/c$ (14) [50]), and a PED pattern from such a crystal is shown in Fig. 7(b). When it comes to Layer 3, several patterns were consistent with the θ-Fe_4Al_{13} phase ($FeAl_3$, $a = 15.49$; $b = 8.08$; $c = 12.47$ [Å], $\beta = 107.7°$; $C2/m$ (12) [51]), as shown in Fig. 7(c). However, in one lamella, in addition to patterns consistent with θ-Fe_4Al_{13}, several patterns from Layer 3 were consistent with the phase τ_{11}-Al_5Fe_2Si ($Al_4Fe_{1.7}Si$, $a = 7.51$; $c = 7.59$ [Å]; $P6_3/mmc$ (194) [52]), as displayed in Fig. 7(d). Patterns from the main phase in Layer 4 fit the η-Fe_2Al_5 phase ($a = 7.66$; $b = 6.42$; $c = 4.22$ [Å]; $Cmcm$ (63) [53]), as shown in Fig. 7(e).

3.3. Density functional theory calculations

The elastic properties of the IMPs identified by TEM were calculated based on first principles. The results in terms of Young's modulus, E,

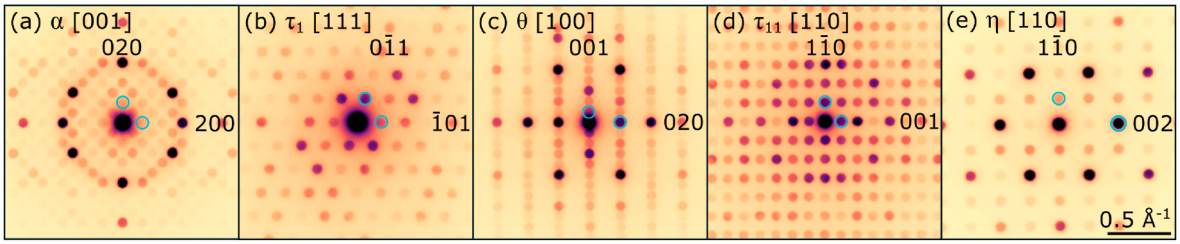

Fig. 7. Precession electron diffraction (PED) patterns from the identified IMPs. **(a)** α_c-$Al_{15}(Fe,Cr,Mn)_3Si_2$ at zone axis [001], **(b)** τ_1-$FeNiAl_9$ at zone axis [111], **(c)** θ-Fe_4Al_{13} at zone axis [100], **(d)** τ_{11}-Al_5Fe_2Si at zone axis [110] and **(e)** η-Fe_2Al_5 at zone axis [110]. In each pattern, *hkl* indices are given for the two spots marked by cyan circles. All patterns share the scale bar shown in (e).

Poisson's ratio, μ, bulk modulus, K, shear modulus, G, and Pugh's ratio, K/G, are listed in Table 3. A material with lower Pugh's ratio is often more brittle [54], and so Pugh's ratio may in some cases offer a simple measure of brittleness. However, Pugh's ratio neglects several aspects, most importantly effects of size and crystal structure [55], and it was included here for comparing the relative brittleness of phases with the same crystal structure.

For the α_c phase, calculations were done for three distinct compositions, including $Al_{96}Fe_{24}Si_{18}$, $Al_{96}Fe_{12}Mn_{12}Si_{18}$ and $Al_{96}Fe_{12}Cr_{12}Si_{18}$. This was done since the compositions estimated by EDS (Table 2) indicated significant amounts of Mn and Cr, and since it is known from previous studies that Fe can be interchanged with other transition elements, such as Mn and Cr, in this phase [27,28,56]. The $Al_{96}Fe_{12}Cr_{12}Si_{18}$ phase had the lowest formation enthalpy with −21.41 eV and was predicted to be the most stable, after $Al_{96}Fe_{12}Mn_{12}Si_{18}$ with −7.36 eV, and $Al_{96}Fe_{24}Si_{18}$ with −6.10 eV. The results given in Table 3 indicated that the α_c phase became both stronger and less brittle by substitution of Fe by Mn or Cr, and that Cr had the most prominent effect.

Since the crystal structure of τ_{11}, as reported in Ref. [52], comprises several partly occupied sites, calculations were done for three structure variants denoted τ_{11}-1 to τ_{11}-3. Amongst these three, τ_{11}-2 had the lowest formation enthalpy (0.03 eV), and was presumably the most stable, followed by τ_{11}-1 (0.19 eV) and τ_{11}-3 (1.31 eV). Further, the τ_{11}-2 variant was predicted to be the softest.

In total, according to Table 3, the phases could be arranged from lower to higher Young's modulus as: α_c-Al-Fe-Si < τ_1 < τ_{11}-2 < α_c-Al-(Fe, Mn)-Si < θ < τ_{11}-1 < α_c-Al-(Fe,Cr)-Si < τ_{11}-3 < η.

3.4. Nanoindentation

Nanoindentation was performed targeting the individual IMP layers in a specimen heat treated at 550 °C for 180 min. Several interface regions were indented, and Fig. 8(a) shows an example BSE SEM image of such a region. All indents were post-examined by SEM to separate the indents that were located exclusively within single layers from those that were located at layer boundaries, so that the latter could be excluded from the final results. In Fig. 8(a), the indents in Al, Layer 1 and steel were all deemed adequately positioned, while only one indent (marked) was positioned within Layer 4 and the remaining at the boundary between Layers 3 and 4. In total, SEM investigations showed 9 – 18 adequately positioned indents for each individual layer. The measurements are presented in Fig. 8, where (b) shows the measured hardness values, and (c) and (d) show the load-displacement curves including and excluding Al and steel, respectively.

Table 4 lists the average hardness, maximum indentation depth and reduced Young's modulus, as calculated from the indentation curves of each layer. According to these results, the layers could be arranged from lower to higher hardness as: Layer 2 (τ_1) < Layer 3 (θ and τ_{11}) < Layer 1 (α_c) < Layer 4 (η with precipitates). Regarding the maximum indentation depth, Layer 3 showed the smallest value, followed by Layer 4, Layer 1 and Layer 2. The reduced Young's modulus is related to the elastic properties of both the sample and the indenter, according to the equation: $1/E_r = (1-\mu_s^2)/E_s + (1-\mu_i^2)/E_i$, where μ_s and E_s are the Poisson's ratio and modulus of the sample and μ_i and E_i those of the indenter [46]. Using the values of 0.07 and 1141 GPa for the Poisson's ratio μ_i and the modulus E_i of the diamond indenter [46], respectively, an estimate for the Young's modulus of each layer could be found. For this, the Poisson's ratio, calculated via DFT, of the dominating IMP in the respective layer was used. The used values and the resulting Young's moduli are listed in Table 4, which indicated that Layer 2 had the lowest modulus, followed by Layer 3, Layer 1 and Layer 4.

Table 3
Mechanical properties calculated based on the DFT results for the phases τ_1-$FeNiAl_9$, τ_{11}-Al_5Fe_2Si and cubic α_c-Al-(Fe,Mn,Cr)-Si with three different compositions; $Al_{96}Fe_{24}Si_{18}$, $Al_{96}Fe_{12}Mn_{12}Si_{18}$ and $Al_{96}Fe_{12}Cr_{12}Si_{18}$. Results for θ-Fe_4Al_{13} and η-Fe_2Al_5 are reported from a previous study [57]. Young's modulus, E, Poisson's ratio, μ, bulk modulus, K, shear modulus, G, and Pugh's ratio, K/G, are listed.

Phase	E [GPa]	μ	K [GPa]	G [GPa]	K/G
τ_1-$FeNiAl_9$	140.2	0.13	62.9	62.1	1.01
α_c-$Al_{96}Fe_{24}Si_{18}$	139.2	0.11	58.7	63.0	0.93
α_c-$Al_{96}Fe_{16}Mn_8Si_{18}$	173.9	0.19	93.3	73.1	1.28
α_c-$Al_{96}Fe_{16}Cr_8Si_{18}$	196.1	0.20	110.2	81.5	1.35
θ-Fe_4Al_{13} [57]	181.8	0.19	96.4	76.7	1.25
τ_{11}-Al_5Fe_2Si-1	187.5	0.21	109.3	77.2	1.42
τ_{11}-Al_5Fe_2Si-2	154.2	0.27	110.5	60.8	1.82
τ_{11}-Al_5Fe_2Si-3	197.1	0.24	127.8	79.3	1.61
η-Fe_2Al_5 [57]	210.2	0.22	126.9	84.8	1.47

3.5. Tensile testing

Tensile testing was done to investigate the influence of the characterised IMP layers on the tensile strengths of the composites. Four miniature tensile specimens were fabricated and tested from composites heat treated at 500 °C for 180 min and at 550 °C for 10 min. Specimens were also attempted fabricated from composites heat treated at 550 °C for 60 min, but all of these fractured during machining. The force-displacement curves are shown in Fig. 9(a), and all specimens showed brittle fracture. For the 500 °C 180 min specimens, the average maximum force was 220 ± 15 N. The inner diameters of the tensile specimens were measured after testing based on SEM images, which resulted in an average and standard deviation of 1.034 ± 0.014 mm. By accounting for the measured diameters of each specimen, the average ultimate tensile strength (UTS) and standard deviation were 262 ± 17 MPa. The 550 °C 10 min specimens showed lower average maximum force and UTS values, amounting to 199 ± 40 N and 239 ± 51 MPa, respectively. However, the scatter in the measured values is large, and the difference in the two average UTS values is lower than the standard deviation.

The fracture surfaces were post-examined by SEM. Fig. 9 shows BSE SEM images of the fracture surfaces from a (b) 500 °C 180 min specimen, (c) 550 °C 10 min specimen, and (d) 550 °C 60 min specimen. All of the three images show the bottom fracture surface referring to the illustration in Fig. 1. In Fig. 9(b), both steel and Al regions can be seen, appearing white and dark grey respectively, in addition to some regions showing intermediate contrast. This indicated that the fracture had propagated through both Al, IMP and steel regions in the 500 °C 180 min specimen. Fig. 9(c) shows large areas of dark and medium contrast, which indicated that the fracture had mainly propagated through Al and IMP regions in the 550 °C 10 min specimen. An even flatter appearance with only speckles of dark contrast can be seen in Fig. 9(d). This indicated that in the 550 °C 60 min specimen, the fracture had mainly ran through the IMP layer and close to the Al-IMP interface in minor areas only.

4. Discussion

4.1. Intermetallic phase formation sequence

4.1.1. Layer 1

Layer 1 that formed first was identified to be composed of the α_c-$Al_{15}(Fe,M)_3Si_2$ phase. The Si contained within α_c was believed to primarily originate from the Al alloy and to diffuse relatively fast to the Al-steel interface during heat treatment. Since the enthalpy of mixing is more negative for Fe-Si than Al-Si [58], this presumably provided a driving force for Si segregation to the Al-steel interface. Formation of α_c followed, since this phase is the most Al-rich phase reported in the Al-Fe-Si-M system that allows $\gtrsim$9 at.% Si [59]. The α_c-Al interface was more irregular than the α_c-steel interface, which suggested that α_c initially grew predominantly into the Al side. This is consistent with the

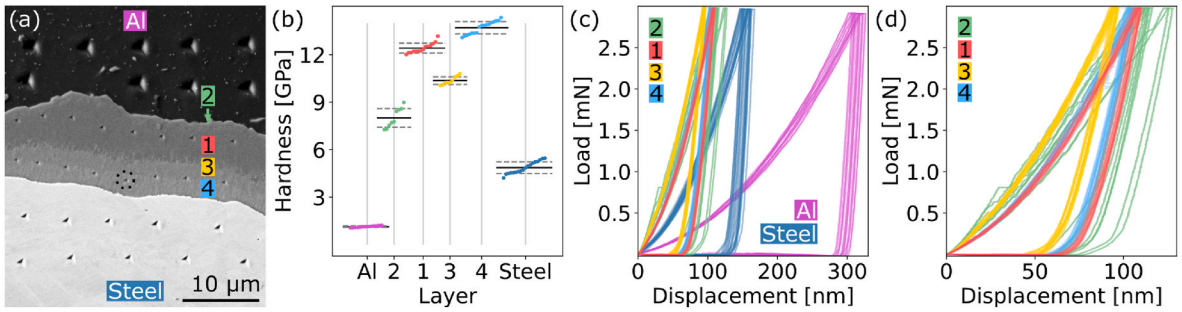

Fig. 8. Nanoindentation of a composite heat treated at 550 °C for 180 min. **(a)** BSE SEM image showing an indented interface region, where all indents from Al, Layer 1 and steel were placed within single layer regions. Several indents were located near the boundary between Layers 3 and 4 and were excluded from the final results, except for the one marked with a black dashed circle. **(b)** Measured hardness values from all indents located within single layer regions. The black lines show average values, while the dashed grey lines show plus and minus one standard deviation. **(c)** and **(d)** Load-displacement curves including and excluding Al and steel, respectively.

Table 4
Nanoindentation of Al, steel and the four IMP layers in a 6082-316L composite heat treated at 550 °C for 180 min. The average hardness, H, maximum indentation depth, h_{max}, and reduced Young's modulus, E_r, are given with plus and minus one standard deviation. In addition, the Poisson's ratio, μ_s, used to calculate the estimated Young's modulus of the sample, E_s, is also given together with the resulting E_s values.

Layer	H [GPa]	h_{max} [nm]	E_r [GPa]	μ_s	E_s [GPa]
Al	1.14 ± 0.05	317 ± 6	95.7 ± 3.1	0.3	95
2	8.01 ± 0.59	116 ± 7	166.8 ± 9.0	0.13	192
1	12.41 ± 0.31	109 ± 1	206.7 ± 3.3	0.20	242
3	10.36 ± 0.24	96 ± 1	185.8 ± 1.7	0.19	214
4	13.69 ± 0.39	106 ± 1	210.1 ± 4.3	0.22	245
Steel	4.86 ± 0.37	157 ± 5	215.2 ± 9.6	0.3	241

solid solubility of Al in Fe exceeding that of Fe in Al [1].

STEM EDS (Table 2) indicated that the major constituents were Al, Fe and Si, together with 4 at.% Cr and ≲2 at.% Mn. As the α_c phase layer grew, the Mn content decreased from 2 to <1 at.% (Table 2), due to the limited supply of Mn, while the Cr content remained unchanged due the high amount of Cr available from 316L. It has been reported that transition elements M, such as Mn and Cr, may substitute for Fe in α_c-$Al_{15}(Fe, M)_3Si_2$ [27,28,56,60,61], leading to the formation of cubic α_c-Al-(Fe, M)-Si instead of hexagonal α_h-Al-Fe-Si that would be expected to form otherwise. The α_c phase is expected to have space group $Im\bar{3}$ [49] for high Fe/M-ratios (~1 – 5 [61,62]), and $Pm\bar{3}$ [63] (also referred to as τ_9, α-Al-Mn-Si) for low (≲1 [61,62,64]). Here, PED showed $Im\bar{3}$ (Fig. 7(b)), which was consistent with the Fe/(Mn + Cr)-ratio being in the range of 3 – 4 (Table 2). The α_c phase has also been identified at other Al-steel interfaces in the presence of Mn and/or Cr [17,25,30,31,65–67], consistent with the phase identification done here.

At an early stage however, a ~10 nm thick Si-rich layer was found at the α_c-steel interface (Fig. 4), and the significance of this layer is not known. In a recent study, scanning electron diffraction of a 10 – 50 nm thick Al-Fe-Si IMP layer indicated the presence of α_c together with (an) other crystal structure(s) that could not be identified [66]. Clearly, more research is needed to understand the initial nanoscale phase formation and growth at Al-steel interfaces, especially in the presence of several alloying elements.

4.1.2. Layer 2

The next IMP layer to form was composed of the τ_1-$FeNiAl_9$ phase (Figs. 5 and 7(a)). The estimated compositions (Table 2) indicated an Al content of 77 – 80 at.%, which fit relatively well with that expected (~82 at.%). The metastable phases Fe_2Al_9 [68] and η-Ni_2Al_9 [69]) are isomorphous, with Fe and Ni being interchangeable ($Fe_{2-x}Ni_xAl_9$ [50]). The Ni contained within τ_1 was believed to have diffused from the steel and through α_c, which contained only ≲1 at.% Ni, to reach the Al side. The growth of τ_1 at the α_c-Al interface can be explained based on the high Al content (~82 at.%) that surpasses other Al-Fe-Ni-Si phases [70], including the α_c phase (~73 at.%). This implies that the Al content was sufficiently high to promote growth of the τ_1 phase first near the Al-α_c interface, and not at the α_c-steel interface. In addition, the enthalpy of mixing is significantly more negative for Al-Ni than Fe-Ni [58], which was expected to provide a driving force for Ni segregation towards the Al interface. In Al-steel bonding, the τ_1-$FeNiAl_9$ phase has only been reported in a few studies [37,71], while the η-Ni_2Al_9 and the Fe_2Al_9 phase have been reported at Al-Ni [72–74] and at Al-Fe interfaces [75], respectively. Some τ_1 crystals displayed facets towards Al, which hinted to a possible crystallographic relationship. Such relationships have been found for Ni_2Al_9 crystals embedded in the Al matrix [76], and this could

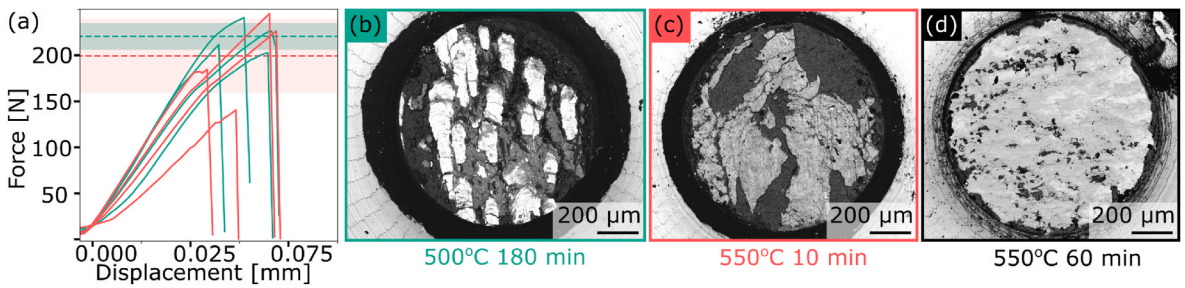

Fig. 9. Tensile testing of heat treated 6082-316L composites. **(a)** Force-displacement curves for four specimens heat treated at 500 °C for 180 min, plotted in green, and four heat treated at 550 °C for 10 min, plotted in red. The average maximum force values are indicated with a dashed green and a dashed red line, respectively, while the red and green areas indicate plus and minus one standard deviation from the average values. BSE SEM images of the fracture surfaces of composites heat treated at **(b)** 500 °C for 180 min, **(c)** 550 °C for 10 min and **(d)** 550 °C for 60 min. In the BSE SEM images, steel appears white or light grey, Al appears black or dark grey and IMPs appear medium grey.

be investigated further for τ_1.

4.1.3. Layer 3

Following prolonged interdiffusion, the Si/Al-ratio in the α_c phase layer decreased (Table 2) due to limited availability of Si. Upon depletion of Si in α_c, phases allowing lower Si contents formed at the interface to steel. Consequently, Layer 3 formed (Fig. 6), for which PED demonstrated the two phases θ and τ_{11} (Fig. 7(c) and (d)). The estimated Si content (~6 at.%, Table 2) laid on the Si-rich side compared to previously reported Si contents in θ of up to ca. 5.5 at.% at 550 °C [21], and oppositely on the Si-lean side of the reported Si contents for τ_{11} of 9 – 12 at.% at 800 °C [22]. This could support possible co-existence of θ and τ_{11} in Layer 3. Further, EDS (Table 2) showed that Layer 3 contained minor amounts of Ni (~2 at.%) and Cr (~5 at.%). The θ phase has been found to incorporate up to 8.9 at.% Ni at 627 °C [77] and 6.4 at.% Cr at 1000 °C [78], which likely are higher than the solubility limits at 550 °C. All the same, the estimated sum of Fe, Ni and Cr of 24 at.% corresponded well to the reported Fe-contents of both the θ (23 – 25 at.% Fe [23,79]) and the τ_{11} phase (23 – 29 at.% Fe [21,80]). Numerous previous studies have reported the θ phase [7,9], including studies on joints with stainless steels where the θ phase contained Ni and Cr [33,34], similar to what was found here.

In contrast to the θ phase, the τ_{11} phase has been scarcely reported. One study revealed τ_{11} inclusions in the η phase layer [81], while another revealed co-existence of τ_{11} with the α_h and η phases [82]. It should be noted that τ_{11} is similar to another phase, τ_{10}, when it comes to both composition (13.3 – 15.5 at.% Si and 24.2 – 25.0 at.% Fe [21,79]) and lattice parameters (hexagonal; $a = 15.52$ Å and $c = 7.30$ Å [21]). The τ_{10} phase has also been reported to form at Al-steel interfaces, and one study reported the disappearance of θ and α_h as τ_{10} and τ_2 appeared after prolonged annealing [19], while in other studies τ_{10} was found near the θ layer [26,83]. Only the τ_{10} phase can be found in the Al-Fe-Si phase diagram at 550 °C, while τ_{11} can be seen first at higher temperatures [21,22,80]. The DFT calculations gave slightly positive formation enthalpy values for the τ_{11} variants used here, with solid solution in Al as reference. This indicated that the τ_{11} phase is not stable if formed in Al, in agreement with the phase diagram. Here, local temperature or composition variations, together with the presence of other alloying elements could have promoted the formation of τ_{11}. It must be emphasised that τ_{11} was observed together with θ in one TEM lamella only, while solely θ was found in another lamella. Future studies are needed to understand the interplay between θ and τ_{11} (and τ_{10}) when several alloying elements participate.

4.1.4. Layer 4

Layer 4 grew at the interface towards steel following prolonged interdiffusion (Fig. 6). This layer had a fine microstructure with numerous small η phase grains, as determined by diffraction (Fig. 7(e)). The estimated compositions (Table 2) indicated an (Al + Si)/(Fe + Ni + Cr)-ratio of 2.4, and although the precipitates contributed to an unknown degree, this ratio laid within the Al/Fe-ratios of 2.3 – 2.6 reported for the η phase in the Al-Fe phase diagram at 550 °C [1]. An η phase layer containing significant amounts of Cr and Ni has been reported in previous studies on aluminised stainless steels [33,34], consistent with the results found here. Layer 4 contained numerous precipitates rich in Cr-Si or Ni, both possibly also containing Al and/or Fe (Fig. 6). Precipitates could be expected in the η phase layer, since the estimated amounts of 3 at.% Ni and 5 at.% Cr (Table 2) exceeded the reported solubility limits of 1 at.% Ni at 850 °C [50] and 3 at.% Cr at 700 °C [84], respectively. Several candidate Ni(-Al)(-Fe) [50,59,77] and Cr-Si(-Al)(-Fe) [84] phases have been identified previously. Precipitates within the η phase layer have been reported frequently, most often identified as precipitates of the τ_1-$Al_2Fe_3Si_3$ phase [19,25], and in some cases as Al-Cr phases [39] or as Ni-rich phases [36].

4.2. Intermetallic phase layer growth rate

The total thicknesses of the interfacial IMP layers in 1080-S355 and 6082-316L composites subjected to various heat treatments were measured (Fig. 2). It was assumed that the total layer growth mainly followed diffusion limited growth characteristics, as reported previously for Al-Fe IMP layers [7,8]. The growth rate constants obtained for the 1080-S355 composites (0.26, 1.17 and 2.59 $\mu m^2 s^{-1}$ at 450, 500 and 550 °C) were high compared to previously reported values. For instance, constants of 0.03 and 0.02 $\mu m^2 s^{-1}$ were obtained for total IMP layer growth at 450 and 500 °C, respectively, in a friction stir welded pure Al-steel joint [2]. Moreover, a constant of 0.00016 $\mu m^2 s^{-1}$ was reported for η phase layer growth at 550 °C in a pure Al-Fe diffusion bonding couple [85]. Most likely, higher growth rates were obtained here due to the strong plastic deformation occurring in both the steel and the Al during roll bonding, which was expected to increase the density of crystal defects offering rapid diffusion pathways.

For the 6082-316L 550 °C composites, the fit line assuming diffusion limited growth did not intersect the origin. This indicated that diffusion limited growth occurred first after an initial incubation time period, during which reaction controlled growth possibly occurred [48]. This has been reported for a joint between pure Al and stainless steel where an oxide layer initially covered the interface and an initial time period was needed for fragmentation of this layer [39]. Here, oxide fragments were seen near the Al-IMP interface (Figs. 4 and 6), that could result from a fragmented surface layer or entrapped air. Further studies are needed to fully understand the role of the oxide layer for the 6082-316L specimens.

Most importantly, the IMP layer growth rates were significantly reduced for the 6082-316L composites compared to the 1080-S355 composites (Fig. 2). In the 6082-316L specimens, the first formed Layer 1, that consisted of the α_c-Al-(Fe,*M*)-Si phase, was the thickest layer and dominated the IMP layer growth. In the 1080-S355 composites however, Layer ii composed of the η-Fe_2Al_5 phase dominated, in accordance with previous results [7,19]. The reduction in growth rate implied that interdiffusion proceeded significantly slower through the α_c phase layer than through the θ and η phase layers that did not contain Si. These findings are supported by a similar study on rolled Al-steel composites where the Al alloy contained 1.2 wt% Si, and where it was found that Fe diffusion through the first formed Al-Fe-Si phase limited the growth rate even after subsequent formation of θ and η [14]. In that study, the first formed Al-Fe-Si phase was described as cubic Fe_3SiAl_{12} ($a = 12.548$ Å) [14], which highly resembled α_c. Furthermore, the formation of porosity on the Al-IMP interface after prolonged annealing (Fig. 3(b)), implied that Al diffused faster through the IMP layers than Fe. This is consistent with previous studies on Al-Fe IMP layers reporting Kirkendall porosity on the Al side [2,8]. Thus, retarded Fe diffusion through α_c was likely the main factor contributing to the reduced growth observed here.

Moreover, the η-steel interface was irregular with elongated grains sticking into the steel side for the 1080-S355 composites (Fig. 3(a)). Such an interface appearance has been reported frequently [7,33] and has been explained based on partly occupied lattice sites in the η phase facilitating fast diffusion along the *c*-direction [86]. This typically leads to textured and columnar η grains after prolonged interdiffusion [6,10]. In the 6082-316L composites, the η-steel interface was much flatter. Several studies have shown that addition of alloying elements may affect the η phase layer by reducing its growth rate and suppressing the strong directional growth, resulting in a flatter interface. This has been reported for both Si additions to Al [15,17,19,86–89], and for Ni [33] and/or Cr [25,32] additions to steel. All of these elements presumably contributed here to reduce the growth rate of the η phase layer and to make the steel interface more planar.

4.3. Mechanical properties

In Layer 1, α_c was the only identified phase, and as this layer grew, the Mn content decreased, while the Cr content remained at ~4 at.%. Three α_c phase variants with different compositions, α_c-Al-Fe-Si, α_c-Al-(Fe,Mn)-Si, and α_c-Al-(Fe,Cr)-Si, were subjected to DFT calculations. The calculations predicted the α_c-Al-(Fe,Cr)-Si phase to be the most stable of the α_c variants, and indicated that the strength increased and the brittleness decreased by substituting Fe with Cr in α_c. Further, the DFT results predicted that the α_c-Al-(Fe,Cr)-Si phase was amongst the phases with the highest Young's modulus. This corresponded well to the nanoindentation results, which showed that Layer 1 had the highest estimated Young's modulus after Layer 4 (Table 4). The hardness and reduced modulus of Layer 1 were measured to 12.41 ± 0.31 GPa and 206.7 ± 3.3 GPa, respectively, which were higher than previously measured values of 10.82 GPa and 175.3 GPa for the α_c-Al-(Fe,Mn)-Si phase [90]. This agreed with the results from DFT indicating modulus increase with substitution of Fe by Cr in α_c.

Layer 2 was discontinuous and thin (~1 μm) even after 180 min at 550 °C, which meant that the nanoindentation measurements could possibly be influenced by the adjacent Al and/or α_c. To minimise the spread in the measurements, the indents were post-examined to include only indents solely placed within Layer 2, as seen in SEM images. The nanoindentation results showed that Layer 2 was the softest layer with the lowest estimated modulus (Table 4), in agreement with the DFT calculations which predicted the τ_1-$FeNiAl_9$ phase to have the lowest Young's modulus after α_c-Al-Fe-Si (Table 3). The measured hardness and reduced modulus of 8.01 ± 0.59 GPa and 166.8 ± 9.0 GPa, respectively, agreed well with previous measurements of 7.71 GPa and 161.5 GPa [90]. Further, Layer 2 showed the largest maximum indentation depth, which indicated that it was the least brittle.

Layer 3 was the second softest layer according to the nanoindentation (Table 4). In this layer, the two phases θ-Fe_4Al_{13} and τ_{11}-Al_5Fe_2Si were identified. Previous studies have reported measured hardness values for the θ phase of 7 GPa [91] and 835 HV (corresponding to 8.2 GPa), the latter for θ containing 7 wt% Si [35]. This is lower than the values measured here, and it is possible that the Cr and Ni content increased the hardness of θ and/or that the presence of τ_{11} affected the hardness of this layer. Based on DFT, the variant τ_{11}-2 was expected to be the most stable and the weakest amongst the τ_{11} variants investigated here (Table 3). The θ phase and the τ_{11}-2 variant both had lower DFT calculated Young's moduli than the η and α_c-Al-(Fe,Cr)-Si phases. This agreed well with Layer 3 having lower estimated modulus than Layer 4 (η with precipitates) and Layer 1 (α_c) based on nanoindentation. However, Layer 3 showed the lowest maximum indentation depth, which indicated that it was the most brittle layer.

Layer 4, in which the η-Fe_2Al_5 phase was the main phase identified, was clearly the hardest and had the highest estimated modulus (Table 4). Also, based on the DFT results (Table 3, [57]), it could be concluded that the η-Fe_2Al_5 phase had the highest Young's modulus. Previously, hardness values for η have been reported to 1100 $HV_{0.05}$ [92] (10.8 GPa), 1000 $HV_{0.025}$ [9] (9.8 GPa), 8 GPa [91], and 9.8 ± 0.9 GPa for a layer of η with Al-Cr phases [39]. In this work, the reduction in grain size combined with the presence of numerous nanoscale precipitates presumably increased the hardness of Layer 4. Further, Layer 4 had the second lowest maximum indentation depth and was thus presumably the second most brittle layer.

Tensile testing of the 550 °C 10 min specimens gave slightly lower average UTS and greater standard deviation than the 500 °C 180 min specimens (Fig. 9(a)). The difference between the two in terms of the IMP layer was that the 500 °C 180 min specimens only contained Layer 1 (α_c) with a thickness of 0.25 ± 0.07 μm, while the 550 °C 10 min specimens contained a continuous ~0.8 μm thick Layer 1 and a discontinuous ≲0.5 μm thick Layer 2 (τ_1). It is well known that the strength of Al-steel joints may increase with reduction in IMP layer thickness [3–5]. Thus, the lower strength was believed to result from the thicker IMP layer, while the larger spread in the measured UTS values could be connected to the uneven growth of Layer 2.

The 550 °C 60 min tensile specimens all failed during machining, which implied that they had lower fracture toughness and possibly lack of bonding. The fracture surfaces (Fig. 9(c)) indicated that the fracture ran mainly through the IMP layer. In contrast to the other tensile specimens, the 550 °C 60 min specimens contained Layer 4 and Layer 3, which were the most brittle IMPs judging by the maximum indentation depths (Table 4). Further, some dark Al regions were seen on the fracture surfaces, which were believed to result from fracture running along the pores observed along the Al-IMP interface (Fig. 3(b)). Altogether, the main reasons for the lower toughness of the 550 °C 60 min specimens were believed to be the thick and brittle IMP layer and the porosity.

5. Summary and conclusions

Formation and growth of interfacial IMPs were investigated after solid-state interdiffusion in rolled steel-Al-steel composites made from Al alloy 6082 and stainless steel 316L. SEM and TEM were utilised for phase identification. DFT calculations and nanoindentation measurements were performed to assess the mechanical properties of the identified phases and the four formed IMP layers (Layer 1 – 4), respectively. The findings can be summarised as follows.

i. During interdiffusion, Si first segregated to the Al-steel interface, before a continuous layer (Layer 1) of α_c-$Al_{15}(Fe,Cr,Mn)_3Si_2$ phase grains formed, creating an irregular interface to Al.
ii. Layer 2 formed subsequently at the Al-α_c interface. This layer was discontinuous and consisted of frequently faceted τ_1-$FeNiAl_9$ grains.
iii. Layer 3 was composed of elongated θ-Fe_4Al_{13} grains and some τ_{11}-Al_5Fe_2Si grains, and contained minor amounts of Si, Cr and Ni.
iv. A fourth layer (Layer 4) formed at the IMP-steel interface that was composed of numerous small grains of mainly the η-Fe_2Al_5 phase, together with nanoscale precipitates, some rich in Cr and Si, and some rich in Ni.
v. Miniature tensile tests confirmed that heat treatments leading to thicker IMP layers and porosity reduced the bond strength and caused brittle interfacial fracture.
vi. Nanoindentation showed that the formed layers could be arranged after increasing hardness and modulus as: Layer 2 (τ_1) < Layer 3 (θ and τ_{11}) < Layer 1 (α_c) < Layer 4 (η with precipitates). Judging by the maximum indentation depth, Layer 3 was indicated to be the most brittle, followed by Layer 4, Layer 1 and Layer 2.
vii. The results from the DFT calculations largely agreed with those from nanoindentation, and the main IMPs could be arranged from lower to higher Young's modulus as: $\tau_1 < \tau_{11} < \theta <$ α_c-Al-(Fe,Cr)-Si $< \eta$. In addition, the results indicated that substitution of Fe by Mn or Cr in the α_c phase leads to higher strength and lower brittleness. Cr substitution had the most prominent effect and also stabilised α_c.
viii. The growth rate of the total IMP layer was markedly reduced for the 6082-316L composites compared to a low alloyed 1080-S355 reference combination. This was believed to primarily result from impeded Fe diffusion through the first formed α_c phase relative to the diffusion through the θ and η phases in the 1080-S355 composites. The significant reduction in growth rate demonstrates the strong influence of alloying elements in both Al and steel.

CRediT author statement

T. Bergh: Conceptualization, Investigation, Formal analysis, Visualization, Writing - Original Draft. S.M. Arbo: Conceptualization, Investigation, Formal analysis, Writing - Review & Editing. A.B. Hagen:

Investigation, Formal analysis. J. Blindheim: Investigation, Formal analysis. J. Friis: Investigation, Formal analysis. M.Z. Khalid: Investigation, Formal analysis. I.G. Ringdalen: Investigation, Formal analysis. R. Holmestad: Conceptualization, Supervision. I. Westermann: Conceptualization, Supervision. P.E. Vullum: Conceptualization, Supervision.

Declaration of competing interest

The authors declare that they have no known competing financial interests or personal relationships that could have appeared to influence the work reported in this paper.

Acknowledgements

The authors acknowledge the contribution of Mustafa Stanikzai for performing heat treatments and initial SEM imaging of the heat treated composites. The support from the Research Council of Norway to SFI Manufacturing (237900), NORTEM (197405) and NorFab (245963/F50) is acknowledged. The DFT calculations were carried out on the Sigma2 high performance clusters (nn9158k).

Appendix A. Supplementary data

Supplementary data to this article can be found online at https://doi.org/10.1016/j.intermet.2021.107443.

References

[1] X. Li, A. Scherf, M. Heilmaier, F. Stein, The Al-rich part of the Fe-Al phase diagram, J. Phase Equilibria Diffus. 37 (2) (2016) 162–173, https://doi.org/10.1007/s11669-015-0446-7, 15477037.

[2] H. Springer, A. Kostka, J.F. dos Santos, D. Raabe, Influence of intermetallic phases and Kirkendall-porosity on the mechanical properties of joints between steel and aluminium alloys, Mater. Sci. Eng. 528 (13–14) (2011) 4630–4642, https://doi.org/10.1016/j.msea.2011.02.057.

[3] R. Borrisutthekul, T. Yachi, Y. Miyashita, Y. Mutoh, Suppression of intermetallic reaction layer formation by controlling heat flow in dissimilar joining of steel and aluminum alloy, Mater. Sci. Eng. 467 (1–2) (2007) 108–113, https://doi.org/10.1016/j.msea.2007.03.049.

[4] T. Tanaka, T. Morishige, T. Hirata, Comprehensive analysis of joint strength for dissimilar friction stir welds of mild steel to aluminum alloys, Scripta Mater. 61 (7) (2009) 756–759, https://doi.org/10.1016/j.scriptamat.2009.06.022.

[5] R. Hatano, T. Ogura, T. Matsuda, T. Sano, A. Hirose, Relationship between intermetallic compound layer thickness with deviation and interfacial strength for dissimilar joints of aluminum alloy and stainless steel, Mater. Sci. Eng., A 735 (2018) 361–366, https://doi.org/10.1016/j.msea.2018.08.065.

[6] N. Chen, M. Wang, H.P. Wang, Z. Wan, B.E. Carlson, Microstructural and mechanical evolution of Al/steel interface with Fe2Al5 growth in resistance spot welding of aluminum to steel, J. Manuf. Process. 34 (June) (2018) 424–434, https://doi.org/10.1016/j.jmapro.2018.06.024, 15266125.

[7] K. Bouché, F. Barbier, A. Coulet, Intermetallic compound layer growth between solid iron and molten aluminium, Mater. Sci. Eng. 249 (1–2) (1998) 167–175, https://doi.org/10.1016/s0921-5093(98)00573-5.

[8] S. Kobayashi, T. Yakou, Control of intermetallic compound layers at interface between steel and aluminum by diffusion-treatment, Mater. Sci. Eng. 338 (1–2) (2002) 44–53, https://doi.org/10.1016/S0921-5093(02)00053-9, 9215093.

[9] A. Bahadur, O.N. Mohanty, Structural studies of hot dip aluminized coatings on mild steel, Mater. Trans., JIM 32 (11) (1991) 1053–1061, https://doi.org/10.2320/matertrans1989.32.1053.

[10] N. Takata, M. Nishimoto, S. Kobayashi, M. Takeyama, Crystallography of Fe2Al5 phase at the interface between solid Fe and liquid Al, Intermetallics 67 (2015) 1–11, https://doi.org/10.1016/j.intermet.2015.07.011, 0966–9795.

[11] P. Huilgol, K.R. Udupa, K.U. Bhat, Metastable microstructures at the interface between AISI 321 steel and molten aluminum during hot-dip aluminizing, Surf. Coating. Technol. 348 (March) (2018) 22–30, https://doi.org/10.1016/j.surfcoat.2018.05.013, 2578972.

[12] W. O, E. Gebhardt, Reaktionen von festem Eisen mit Schmelzen aus Aluminium und Aluminiumlegierungen, ZeitschriftfürMetallkunde 12 (1936) (1953) 44–154.

[13] D.I. Layner, A.K. Kurakin, Mechanism of the influence of silicon in aluminium on the reaction diffusion of iron, Fiz. metal. metalloved. 18 (1) (1964) 145–148.

[14] A.K. Kurakin, Mechanism of the influence of silicon on the process of the reaction diffusion of iron in aluminium, Fiz. metal. metalloved. 30 (1) (1970) 105–110.

[15] G. Eggeler, W. Auer, H. Kaesche, On the influence of silicon on the growth of the alloy layer during hot dip aluminizing, J. Mater. Sci. 21 (1986) 3348–3350.

[16] M. Akdeniz, A. Mekhrabov, T. Yilmaz, The role of Si addition on the interfacial interaction in Fe-Al diffusion layer, Scripta Metall. etMaterialia 3 (12) (1994) 1723–1728.

[17] L.A. Jacome, S. Weber, A. Leitner, E. Arenholz, J. Bruckner, H. Hackl, A.R. Pyzalla, Influence of filler composition on the microstructure and mechanical properties of steel - aluminum joints produced by metal arc joining, Adv. Eng. Mater. 11 (5) (2009) 350–358, https://doi.org/10.1002/adem.200800319.

[18] J.L. Song, S.B. Lin, C.L. Yang, C.L. Fan, Effects of Si additions on intermetallic compound layer of aluminum-steel TIG welding-brazing joint, J. Alloys Compd. 488 (1) (2009) 217–222, https://doi.org/10.1016/j.jallcom.2009.08.084, 9258388.

[19] H. Springer, A. Kostka, E.J. Payton, D. Raabe, A. Kaysser-Pyzalla, G. Eggeler, On the formation and growth of intermetallic phases during interdiffusion between low-carbon steel and aluminum alloys, Acta Mater. 59 (4) (2011) 1586–1600, https://doi.org/10.1016/j.actamat.2010.11.023.

[20] G. Ghosh, Aluminium-Iron-Silicon (Iron Systems, Part 1), 11D1, *SpringerMaterials Landolt-Börnstein - Group IV Physical Chemistry*, 2008, pp. 1–83, https://doi.org/10.1007/978-3-540-69761-9_11.

[21] N. Krendelsberger, F. Weitzer, J.C. Schuster, On the reaction scheme and liquidus surface in the ternary system Al-Fe-Si, Metall. Mater. Trans. 38 (August) (2007), https://doi.org/10.1007/s11661-007-9182-x.

[22] M.C.J. Marker, B. Skolyszewska-Kühberger, H.S. Effenberger, C. Schmetterer, K. W. Richter, Intermetallics Phase equilibria and structural investigations in the system Al-Fe-Si, Intermetallics 19 (12) (2011) 1919–1929, https://doi.org/10.1016/j.intermet.2011.05.003.

[23] W.-J. Cheng, C.-J. Wang, Observation of high-temperature phase transformation in the Si-modified aluminide coating on mild steel using EBSD, Mater. Char. 61 (4) (2010) 467–473, https://doi.org/10.1016/j.matchar.2010.02.001.

[24] B. Lemmens, H. Springer, M.J. Duarte, I. De Graeve, J. De Strycker, D. Raabe, K. Verbeken, Atom probe tomography of intermetallic phases and interfaces formed in dissimilar joining between Al alloys and steel, Mater. Char. 120 (2016) 268–272, https://doi.org/10.1016/j.matchar.2016.09.008, 10445803.

[25] W.J. Cheng, C.J. Wang, Effect of chromium on the formation of intermetallic phases in hot-dipped aluminide Cr-Mo steels, Appl. Surf. Sci. 277 (2013) 139–145, https://doi.org/10.1016/j.apsusc.2013.04.015, 1694332.

[26] W. Jiang, G. Li, Z. Jiang, Y. Wu, Z. Fan, A. Fe, Effect of heat treatment on microstructures and mechanical properties of Al/Fe bimetal, Mater. Sci. Eng., A 0836 (2018), https://doi.org/10.1080/02670836.2018.1465620.

[27] D. Munson, A clarification of the phases occurring in aluminium-rich aluminium-iron-silicon alloys, with particular reference to the ternary α-AlFeSi, J. Inst. Met. 95 (1967) 217–219.

[28] C.Y. Sun, L.F. Mondolfo, A clarification of the phases occurring in aluminium-rich aluminium-iron-silicon alloys, J. Inst. Met. 95 (1967) 384.

[29] H. Becker, T. Bergh, P.E. Vullum, A. Leineweber, Y. Li, Effect of Mn and cooling rates on α-, β- and δ- Al–Fe–Si intermetallic phase formation in a secondary Al–Si alloy, Materialia 5 (2019), https://doi.org/10.1016/j.mtla.2018.100198.

[30] J. Chen, B. Shalchi Amirkhiz, R. Zhang, B. Rona, On the joint formation and interfacial microstructure of Cold metal transfer cycle step braze welding of aluminum to steel butt joint, Metall. Mater. Trans. 51 (10) (2020) 5198–5212, https://doi.org/10.1007/s11661-020-05917-8, 10735623.

[31] M. Kohlhepp, P.J. Uggowitzer, M. Hummel, H.W. Höppel, Formation of die soldering and the influence of alloying elements on the intermetallic interface, Materials 14 (7) (2021), https://doi.org/10.3390/ma14071580, 19961944.

[32] Y. Li, Q. Jia, Z. Zhu, W. Gao, H. Chen, Growth behaviour of intermetallic layer on stainless steel in aluminium hot-dipping process, Surf. Rev. Lett. 24 (4) (2017) 1–9, https://doi.org/10.1142/S0218625X17500469, 0218625X.

[33] F. Barbier, D. Manuelli, K. Bouché, Characterization of aluminide coatings formed on 1.4914 and 316L steels by hot-dipping in molten aluminium, Scripta Mater. 36 (4) (1997) 425–431, https://doi.org/10.1016/S1359-6462(96)00407-1, 13596462.

[34] V.I. Dybkov, Interaction of 18Cr-10Ni stainless steel with liquid aluminium, J. Mater. Sci. 25 (1990) 3615–3633.

[35] J.L. Song, et al., Analysis of intermetallic layer in dissimilar TIGwelding–brazing butt joint of aluminium alloy to stainless steel, Sci. Technol. Weld. Join. 15 (3) (2010) 213–218, https://doi.org/10.1179/136217110X12665048207610, 13621718.

[36] B. Dangi, T.W. Brown, K.N. Kulkarni, Effect of silicon, manganese and nickel present in iron on the intermetallic growth at iron - aluminum alloy interface, J. Alloys Compd. 769 (2018) 777–787, https://doi.org/10.1016/j.jallcom.2018.07.364, 9258388.

[37] J.H. Lee, J.G. Yun, S.Y. Kwak, C.Y. Kang, Nucleation and growth of intermetallic compounds formed in boron steel hot-dipped in Al-Ni alloy, Coatings 7 (11) (2017) 1–14, https://doi.org/10.3390/coatings7110195, 20796412.

[38] K. Murakami, N. Nishida, K. Osamura, Y. Tomota, T. Suzuki, Aluminization of high purity iron and stainless steel by powder liquid coating, Acta Mater. 52 (8) (2004) 2173–2184, https://doi.org/10.1016/j.actamat.2004.01.009, 13596454.

[39] B. Liu, Q. Yang, Y. Wang, Interaction and intermetallic phase formation between aluminum and stainless steel, Results Phys. 12 (November 2018) (2019) 514–524, https://doi.org/10.1016/j.rinp.2018.11.076, 2211–3797.

[40] F. de la Peña, E. Prestat, V.T. Fauske, P. Burdet, P. Jokubauskas, M. Nord, T. Ostasevicius, K.E. MacArthur, M. Sarahan, D.N. Johnstone, J. Taillon, J. Lähnemann, V. Migunov, A. Eljarrat, J. Caron, T. Aarholt, S. Mazzucco, M. Walls, T. Slater, F. Winkler, Pquinn-dls, B. Martineau, G. Donval, R. McLeod, E. R. Hoglund, I. Alxneit, D. Lundeby, T. Henninen, L.F. Zagonel, A. Garmannslund, Hyperspy/Hyperspy: HyperSpy v1.5.2, *Zenodo*, 2019, https://doi.org/10.5281/ZENODO.3396791.

[41] G. Kresse, J. Furthmüller, Efficient iterative schemes for ab initio total-energy calculations using a planewave basis set, 11 169–11 186, Phys. Rev. B 54 (16) (1996), https://doi.org/10.1103/PhysRevB.54.11169, 1550235X.

[42] P.E. Blochl, Projector augmented-wave method, Phys. Rev. B 50 (24) (1994), https://doi.org/10.1103/PhysRevB.50.17953.

[43] G. Kresse, D. Joubert, Fromultra soft pseudopotentials to the projector augmented-wave method, Phys. Rev. B 59 (3) (1999) 1758–1775, https://doi.org/10.1103/PhysRevB.59.1758, 1550235X.

[44] F. Mouhat, F.X. Coudert, Necessary and sufficient elastic stability conditions in various crystal systems, Phys. Rev. B - Condens. Matter Mater. Phys. 90 (22) (2014) 4–7, https://doi.org/10.1103/PhysRevB.90.224104, 1550235X.

[45] R. Hill, The elastic behaviour of a crystalline aggregate, Proc. Phys. Soc. 65 (5) (1952) 349–354, https://doi.org/10.1088/0370-1298/65/5/307.

[46] W.C. Oliver, G.M. Pharr, An improved technique for determining hardness and elastic modulus using load and displacement sensing indentation experiments, J. Mater. Res. 7 (6) (1992) 1564–1583.

[47] J. Blindheim, Ø. Grong, T. Welo, M. Steinert, On the mechanical integrity of AA6082 3D structures deposited by hybrid metal extrusion bonding additive manufacturing, J. Mater. Process. Technol. 282 (2020), https://doi.org/10.1016/j.jmatprotec.2020.116684.

[48] A. Paul, T. Laurila, V. Vuorinen, S.V. Divinski, Thermodynamics, Diffusion and the Kirkendall Effect in Solids, 2014, https://doi.org/10.1007/978-3-319-07461-0.

[49] M. Cooper, The crystal structure of the ternary alloy α (AlFeSi), Acta Crystallogr. 23 (1967) 1106–1107, https://doi.org/10.1107/S0365110X67004372.

[50] I. Chumak, K.W. Richter, H. Ipser, The Fe-Ni-Al phase diagram in the Al-rich (>50 at.% Al) corner, Intermetallics 15 (11) (2007) 1416–1424, https://doi.org/10.1016/j.intermet.2007.04.012.

[51] J. Grin, U. Burkhardt, M. Ellner, K. Peters, Refinement of the Fe4Al13 structure and its relationship to the quasihomological homeotypical structures, Zeitschrift fur Kristallographie 209 (6) (1994) 479–487, https://doi.org/10.1524/zkri.1994.209.6.479.

[52] N. German, V. Bel'skii, T. Yanson, O. Zarechnyuk, Crystal structure of the compound Fe1.7Al4Si, Sov. Phys. Crystallogr. 34 (3) (1989) 735–737.

[53] U. Burkhardt, Y. Grin, M. Ellner, K. Peters, Structure refinement of the iron–aluminium phase with the approximate composition Fe2Al5, Acta Crystallogr. 50 (3) (1994) 313–316, https://doi.org/10.1107/S0108768193013989.

[54] S. Pugh, XCII. Relations between the elastic moduli and the plastic properties of polycrystalline pure metals, The Lond. Edinb, Dublin Philos. Mag. J. Sci. 45 (367) (1954) 823–843, https://doi.org/10.1080/14786440808520496, 1941–5982.

[55] R.P. Thompson, W.J. Clegg, Predicting whether a material is ductile or brittle, Curr. Opin. Solid State Mater. Sci. 22 (3) (2018) 100–108, https://doi.org/10.1016/j.cossms.2018.04.001, 13590286.

[56] J.E. Tibballs, J.a. Horst, C.J. Simensen, Precipitation of α-Al(Fe,Mn) Si from the melt, J. Mater. Sci. 36 (2001) 937–941, https://doi.org/10.1023/A:1004815621313.

[57] M.Z. Khalid, J. Friis, P.H. Ninive, K. Marthinsen, A. Strandlie, DFT calculations based insight into bonding character and strength of Fe2Al5 and Fe4Al13 intermetallics at Al-Fe joints, Procedia Manuf. 15 (2351) (2018) 1407–1415, https://doi.org/10.1016/j.promfg.2018.07.341, 23519789.

[58] A. Takeuchi, A. Inoue, Calculation of Mixing Enthalpy and Mismatch Entropy, 2000.

[59] H.L. Chen, Q. Chen, Y. Du, J. Bratberg, A. Engström, Update of Al-Fe-Si, Al-Mn-Si and Al-Fe-Mn-Si thermodynamic descriptions, Trans. Nonferrous Metals Soc. China 24 (7) (2014) 2041–2053, https://doi.org/10.1016/S1003-6326(14)63310-0, 10036326.

[60] H. Westengen, Formation of intermetallic compounds during DC casting of a commercial purity Al-Fe-Si alloy, Zeitschrift für Metallkunde 73 (1982) 360–368.

[61] A.L. Dons, Superstructures in α-Al(Mn,Fe,Cr)Si, Zeitschrift für Metallkunde 76 (2) (1985) 151–153.

[62] P. Donnadieu, G. Lapasset, T.H. Sanders, Manganese-induced ordering in the α-(Al-Mn-Fe-Si) approximant phase, Phil. Mag. Lett. 70 (5) (1994) 319–326, https://doi.org/10.1080/09500839408240993, 0950–0839.

[63] M. Cooper, The crystal structure of the ternary alloy α (AlMnSi), Acta Crystallogr. 20 (1966) 614–617, https://doi.org/10.1107/S0365110X67004372.

[64] P. Orozco-Gonzalez, M. Castro-Román, Effect of iron addition on the crystal structure of the α-AlFeMnSi phase formed in the quaternary Al-Fe-Mn-Si system phase formed in the quaternary Al-Fe-Mn-Si system, Revista deMetalurgia 47 (6) (2011) 453–461, https://doi.org/10.3989/revmetalm.1068.

[65] S.M. Arbo, T. Bergh, H. Solhaug, I. Westermann, B. Holmedal, Influence of thermomechanical processing sequence on properties of AA6082-IF steel cold roll bonded composite sheet, Procedia Manuf. 15 (2018) 152–160, https://doi.org/10.1016/j.promfg.2018.07.189.

[66] T. Bergh, L. Sandnes, D. Neal, F. Berto, R. Holmestad, Microstructural and mechanical characterisation of a second generation hybrid metal extrusion bonding aluminium-steel butt joint, Mater. Char. (2021) 110761, https://doi.org/10.1016/j.matchar.2020.110761.

[67] L. Sandnes, T. Bergh, Ø. Grong, R. Holmestad, P.E. Vullum, F. Berto, Interface microstructure and tensile properties of a third generation aluminium- steel ButtWeld produced using the hybrid metal extrusion bonding (HYB) process, Mater. Sci. Eng., A 809 (2021), https://doi.org/10.1016/j.msea.2021.140975, 140975.

[68] C.J. Simensen, R. Vellasamy, Determination of phases present in cast material of an Al-0.5 Wt.% Fe-0.2 Wt.% Si alloy, Z. Metallkd. (1977) 428–431.

[69] X.Z. Li, K.H. Kuo, Decagonal quasicrystals with different periodicities along the tenfold axis in rapidly solidified al-ni alloys, Phil. Mag. Lett. 58 (3) (1988) 167–171, https://doi.org/10.1080/09500838808214749, 13623036.

[70] A.A. Amenova, N.A. Belov, D.U. Smagulov, Computation of liquidus of the Al - Fe -Mn - Ni - Si system in the range of aluminum-nickel alloys (nickalins), Met. Sci. Heat Treat. 56 (3–4) (2014) 137–142, https://doi.org/10.1007/s11041-014-9719-8, 15738973.

[71] W.J. Cheng, C.J. Wang, Characterization of intermetallic layer formation in aluminide/nickel duplex coating on mild steel, Mater. Char. 69 (43) (2012) 63–70, https://doi.org/10.1016/j.matchar.2012.04.007, 10445803.

[72] A.S. Edelstein, R.K. Everett, G.Y. Richardson, S.B. Qadri, E.I. Altman, J.C. Foley, J. H. Perepezko, Intermetallic phase formation during annealing of Al/Ni multilayers, J. Appl. Phys. 76 (12) (1994) 7850–7859, https://doi.org/10.1063/1.357893, 218979.

[73] K. Barmak, C. Michaelsen, G. Lucadamo, Reactive phase formation in sputter-deposited Ni/Al multilayer thin films, J. Mater. Res. 12 (1) (1997) 133–146, https://doi.org/10.1557/JMR.1997.0021, 8842914.

[74] K.J. Blobaum, D. VanHeerden, A.J. Gavens, T.P. Weihs, Al/Ni formation reactions: characterization of the metastable Al9Ni2 phase and analysis of its formation, Acta Mater. 51 (13) (2003) 3871–3884, https://doi.org/10.1016/S1359-6454(03)00211-8, 13596454.

[75] D. Dubaux, Gaudry, M.C. de Weerd, S. Šturm, M. Podlogar, J. Ghanbaja, S. Migot, V. Fournée, M. Sicot, J. Ledieu, Metastable Al-Fe intermetallic stabilised by epitaxial relationship, Appl. Surf. Sci. 533 (July) (2020), https://doi.org/10.1016/j.apsusc.2020.147492, 1694332.

[76] Y.-W. Kim, A.G. Jackson, Phases and orientation relationships in a rapidly solidified Al-6Fe-6Ni alloy, Scripta Metall. 20 (5) (1986) 777–782.

[77] L. Zhang, Y. Du, H. Xu, C. Tang, H. Chen, andW. Zhang, Phase equilibria of the Al-Fe-Ni system at 850 °C and 627 °C, J. Alloys Compd. 454 (1–2) (2008) 129–135, https://doi.org/10.1016/j.jallcom.2006.12.042, 9258388.

[78] M. Palm, The Al–Cr–Fe system–Phases and phase equilibria in the Al-rich corner, J. Alloys Compd. 252 (1997) 192–200.

[79] S.P. Gupta, Intermetallic compound formation in Fe - Al - Si ternary system: Part I, Mater. Char. 49 (2003) 269–291, https://doi.org/10.1016/S1044-5803(03)00006-8.

[80] Y. Du, J. Clemens, Z.-k. Liu, R. Hu, A thermodynamic description of the Al-Fe-Si system over the whole composition and temperature ranges via a hybrid approach of CALPHAD and key experiments, Intermetallics 16 (2008) 554–570, https://doi.org/10.1016/j.intermet.2008.01.003.

[81] B. Lemmens, B. Corlu, J. de Strycker, K. Verbeken, The effect of Si on the intermetallics formation during hot dip aluminizing, Adv. Mater. Res. 922 (2014) 429–434. https://doi.org/10.4028/www.scientific.net/AMR.922.429, 10226680.

[82] P. Malczyk, C. Weigelt, T. Zienert, N. Brachhold, S.O. Sauke, H. Semrau, C. G. Aneziris, Investigation of interfacial phase formation during corrosion of stainless steel, Interceram: Int. Ceram. Rev. 69 (1) (2020) 42–51, https://doi.org/10.1007/s42411-019-0070-3, 205214.

[83] S. Pontevichi, F. Bosselet, F. Barbeau, M. Peronnet, J.C. Viala, Solid-liquid phase equilibria in the Al-Fe-Si system at 727°C, J. Phase Equilibria Diffus. 25 (6) (2004) 528–537, https://doi.org/10.1361/15477020421052.

[84] Z. Zhou, Z. Li, Y. Xie, X. Wang, Y. Liu, Z. Long, F. Yin, Experimental study of the phase relationships in the Al-rich corner of the Al-Si-Fe-Cr quaternary system at 700°C, Int. J. Oper. Res. 106 (5) (2015) 470–480, https://doi.org/10.3139/146.111202, 18625282.

[85] D. Naoi, M. Kajihara, Growth behavior of Fe2Al5 during reactive diffusion between Fe and Al at solid-state temperatures, Mater. Sci. Eng. 459 (1–2) (2007) 375–382, https://doi.org/10.1016/j.msea.2007.01.099, 9215093.

[86] J.E. Nicholls, Hot-dipped aluminium coatings, Anti-corrosion Methods & Mater. 11 (10) (1964) 16–21.

[87] H. Azimaee, M. Sarfaraz, M. Mirjalili, K. Aminian, Effect of silicon and manganese on the kinetics and morphology of the intermetallic layer growth during hot-dip aluminizing, Surf. Coating. Technol. 357 (July 2018) (2019) 483–496, https://doi.org/10.1016/j.surfcoat.2018.10.035, 2578972.

[88] H.S. Furuya, Y.T. Sato, Y.S. Sato, H. Kokawa, Y. Tatsumi, Strength improvement through grain refinement of intermetallic compound at Al/Fe dissimilar joint interface by the addition of alloying elements, Metall. Mater. Trans. 49 (2) (2018) 527–536, https://doi.org/10.1007/s11661-017-4442-x, 10735623.

[89] B. Lemmens, H. Springer, I. De Graeve, J. De Strycker, D. Raabe, K. Verbeken, Effect of silicon on the microstructure and growth kinetics of intermetallic phases formed during hot-dip aluminizing of ferritic steel, Surf. Coating. Technol. 319 (2017) 104–109, https://doi.org/10.1016/j.surfcoat.2017.03.040, 2578972.

[90] C.L. Chen, A. Richter, R.C. Thomson, Investigation of mechanical properties of intermetallic phases in multi-component Al-Si alloys using hot-stage nanoindentation, Intermetallics 18 (4) (2010) 499–508, https://doi.org/10.1016/j.intermet.2009.09.013, 9669795.

[91] T. Ogura, K. Ueda, Y. Saito, A. Hirose, Nanoindentation measurement of interfacial reaction layers in 6000 series aluminum alloys and steel dissimilar metal joints with alloying elements * 1, Mater. Trans. 52 (5) (2011) 979–984, https://doi.org/10.2320/matertrans.L-MZ201112.

[92] H. Glasbrenner, J. Konys, K. Stein-Fechner, O. Wedemeyer, Comparison of microstructure and formation of intermetallic phases on F82H-mod. and MANET II, J. Nucl. Mater. 258–263 (PART 2 B) (1998) 1173–1177, https://doi.org/10.1016/S0022-3115(98)00181-0, 223115.